

ARTICLE

Received 23 Jan 2017 | Accepted 12 May 2017 | Published 3 Jul 2017

DOI: 10.1038/ncomms15950

OPEN

Microwave-free nuclear magnetic resonance at molecular scales

James D.A. Wood^{1,†}, Jean-Philippe Tetienne¹, David A. Broadway¹, Liam T. Hall², David A. Simpson², Alastair Stacey^{1,3} & Lloyd C.L. Hollenberg^{1,2}

The implementation of nuclear magnetic resonance (NMR) at the nanoscale is a major challenge, as the resolution of conventional methods is limited to mesoscopic scales. Approaches based on quantum spin probes, such as the nitrogen-vacancy (NV) centre in diamond, have achieved nano-NMR under ambient conditions. However, the measurement protocols require application of complex microwave pulse sequences of high precision and relatively high power, placing limitations on the design and scalability of these techniques. Here we demonstrate NMR on a nanoscale organic environment of proton spins using the NV centre while eliminating the need for microwave manipulation of either the NV or the environmental spin states. We also show that the sensitivity of our significantly simplified approach matches that of existing techniques using the NV centre. Removing the requirement for coherent manipulation while maintaining measurement sensitivity represents a significant step towards the development of robust, non-invasive nanoscale NMR probes.

¹Centre for Quantum Computation and Communication Technology, School of Physics, The University of Melbourne, Melbourne, Victoria 3010, Australia.

²School of Physics, The University of Melbourne, Melbourne, Victoria 3010, Australia. ³Melbourne Centre for Nanofabrication, 151 Wellington Road, Clayton, Melbourne, Victoria 3168, Australia. †Present address: Department of Physics, University of Basel, Klingelbergstrasse 82, 4056 Basel, Switzerland.

Correspondence and requests for materials should be addressed to J.D.A.W. (email: james.wood@unibas.ch) or to J.-P.T. (email: jtetienne@unimelb.edu.au).

The discovery of nuclear magnetic resonance (NMR), and its related technologies, was one of the great scientific achievements of the twentieth century, contributing to significant advances in areas ranging from materials science to healthcare. However, the limitation in sensitivity of traditional induction-based detection has required the development of different detection schemes in order to extend NMR technology to the nanoscale, where the study of processes at the molecular scale is of intense interest. The nitrogen-vacancy (NV) centre in diamond¹ has seen remarkable developments as a high-sensitivity nanoscale magnetometer^{2–10}. In recent years, the NV centre has been utilized to achieve nanoscale NMR at sensitivities close to that required for single-proton detection^{11–16}. Its room-temperature operation also makes it an ideal candidate for biological nano-NMR^{17,18}. However, current NMR protocols using the NV centre require the application of complex, high-power and high-precision microwave pulsing sequences in order to filter the environmental spectrum, placing significant constraints on nano-magnetic resonance imaging applications¹⁹. The application of strong microwave pulses is potentially invasive given the attendant electric fields as an inevitable by-product in the generation of the magnetic control fields²⁰. In addition, achieving such quantum control on a large ensemble of NV centres over a wide field of view²¹, or on a scanning probe microscopy tip^{22–24}, remains a challenge due to the requirement for homogeneity in the driving field. Finally, the adaptability of such high-precision control to dynamic environments such as *in vitro*¹⁷ is unknown.

In this work, we demonstrate microwave-free nano-NMR on a nanoscopic sample of proton nuclear spins within an organic sample external to the diamond. We achieve this via static field tuning to the natural spin interactions between sensor and target, and measure a change in the longitudinal relaxation time, T_1 (ref. 25). The resulting all-optical microwave-free protocol can be applied in a non-invasive manner (for example, through optical excitation constrained within the diamond using total internal reflection²⁶), significantly widening the range of applications where NV-based nano-NMR can be used. We demonstrate the microwave-free NMR technique using both isotopic forms ¹⁴NV and ¹⁵NV, which exhibit different fundamental characteristics in this context, and use the data to estimate the NV-sample distance (10–12 nm for the studied NVs), as well as the number of protons detected ($< 10^5$). In addition, we directly compare our microwave-free nano-NMR to the prevailing microwave control based nano-NMR technique, and find that both approaches offer comparable sensitivity.

Results

Principle of T_1 -based NMR. The microwave-free technique for magnetic resonance spectroscopy is based on T_1 relaxometry detection^{7,27–30} and precise magnetic field tuning to bring the NV into resonance with the Zeeman split target spin transitions^{31–34}. This technique was proposed and demonstrated for quantitative electron spin resonance spectroscopy using an ensemble of NV centres²⁵ and extended to hyperfine-coupled nuclear spin spectroscopy with single NV centres³⁵. The ultimate goal of nano-NMR is the spectroscopic detection of bare nuclear spins in molecular systems (Fig. 1a). Without the assistance of strong hyperfine coupling this is a significant challenge due to the low nuclear magnetic moment^{35,36}. Applying the T_1 -NMR technique to this problem requires the precise tuning of the NV probe to near its ground state level anti-crossing (GSLAC), where the system's dynamics are dominated by a relatively complex landscape of electron–nuclear spin mixing^{36–38}, in order to bring the electronic NV transitions into resonance with the nuclear spin

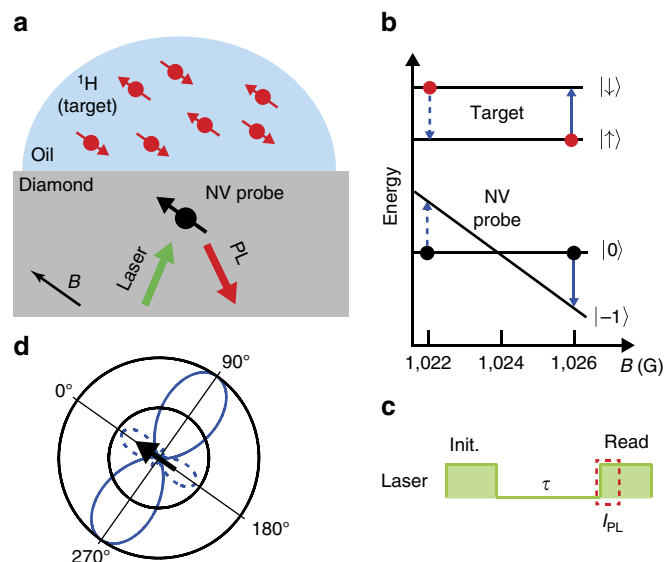


Figure 1 | Principle of microwave-free nano-nuclear magnetic resonance.

(a) Schematic of the experimental setup. The protons within an organic sample external to the diamond are the targets probed by a shallow nitrogen-vacancy (NV) centre. A 532 nm green laser is used to initialize the NV spin while the red photoluminescence (PL) is measured via a single-photon detector. The background magnetic field is aligned with the NV quantization axis with a variable strength, B . (b) Schematic of the energy levels of the NV (spin states $|0\rangle$ and $|-1\rangle$), neglecting the hyperfine structure for clarity and of a target nuclear spin such as ^1H (states $|\uparrow\rangle$ and $|\downarrow\rangle$). As B is swept across the ground state level anti-crossing (GSLAC), two resonances can in principle occur where the NV and target spins can exchange energy via their mutual magnetic dipole–dipole interaction, causing an increase in their respective longitudinal relaxation rate. (c) The measurement sequence consists of laser pulses to initialize and subsequently read out the NV spin state, separated by a wait time τ . (d) Polar plot of the relaxation rate induced by a single spin, $\Gamma_{1,\text{ext}}$, as a function of the angle θ between the quantization axis and the NV–target separation. The solid (dashed) line corresponds to the after-GSLAC (before-GSLAC) resonance. The values are normalized by the global maximum, so that the outer circle corresponds to maximum strength. The polar plot is rotated by $\theta = 54.7^\circ$, which is the angle between an NV below a (100) diamond surface, and the closest target spin on the surface.

transition. At a resonance point (which in principle could occur both before and after the GSLAC as depicted in Fig. 1b), the longitudinal relaxation time T_1 of both the NV centre and the environmental spin(s) are significantly reduced, due to their mutual dipole–dipole interaction^{25,33,35}. To probe these resonances, the strength, B , of a static background magnetic field aligned with the NV quantization axis, is swept near the GSLAC ($B \approx 1,024$ G) and the T_1 decay is optically measured at each corresponding transition frequency.

The transitions associated with two simple resonances before and after the GSLAC are depicted in Fig. 1b. The relaxation rate of the initialized NV spin state $|0\rangle$ to $|-1\rangle$, induced at one of these resonances (over and above the intrinsic relaxation rate $\Gamma_{1,\text{int}}$, assumed constant in the field range considered), is set by the sum of the contributions of all resonant target spins, $\Gamma_{1,\text{ext}}^\pm = \sum_i \Gamma_{1,\text{ext}}^{i,\pm}$. The contribution of each i th spin can be expressed as³⁵

$$\Gamma_{1,\text{ext}}^{i,\pm} = \frac{1}{2\Gamma_2^*} \left(\frac{\mu_0 \gamma_{\text{NV}} \gamma_t \hbar}{4\pi} \right)^2 \left(\frac{3 \sin^2 \theta_i - 1 \pm 1}{r_i^3} \right)^2 \quad (1)$$

where γ_{NV} and γ_t are the gyromagnetic ratios of the NV and

target spins, respectively; θ_i is the polar angle of separation between the two spins relative to the quantization axis; r_i is the separation distance; Γ_2^* is the total dephasing rate of the spin system; μ_0 is the vacuum permeability; \hbar is Planck's constant; and the \pm sign refers to the resonance after (+) and before (−) the GSLAC. Near resonance, the photoluminescence (PL) signal after an evolution time τ is given by (see refs 27,28 and Supplementary Note 1)

$$I_{\text{PL}}(\tau, B) = I_0 \left[1 + C e^{-\Gamma_{1,\text{tot}}(B)\tau} \right], \quad (2)$$

where I_0 is a normalization constant, $C \sim 0.2$ is the PL contrast of the T_1 decay, and the total relaxation rate is²⁵

$$\Gamma_{1,\text{tot}}(B) = \Gamma_{1,\text{int}} + \frac{\Gamma_{1,\text{ext}}^\pm}{1 + \left(\frac{\omega_{\text{NV}}(B) - \omega_t(B)}{\Gamma_2^*} \right)^2}, \quad (3)$$

with ω_{NV} the NV transition frequency and $\omega_t = \gamma_t B$ the Larmor frequency of the target spin, which vary with B as depicted in Fig. 1b. Equation (2) is valid when the intrinsic relaxation ($\Gamma_{1,\text{int}}$) is dominated by magnetic noise acting on the $|0\rangle \leftrightarrow |-1\rangle$ transition, which is generally the case near the GSLAC (Supplementary Note 1). Experimentally, rather than recording a full curve $I_{\text{PL}}(\tau)$, it is generally sufficient to probe a single, well chosen value of τ , from which one can retrieve $\Gamma_{1,\text{tot}}(B)$ using

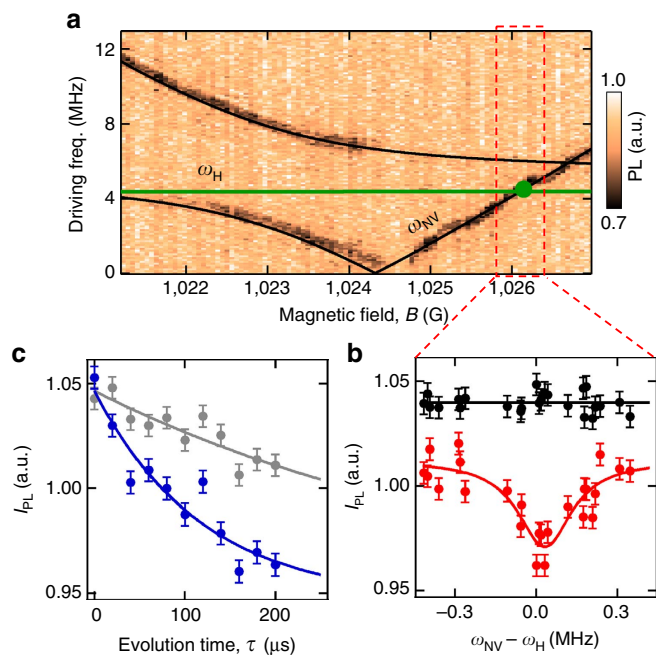


Figure 2 | Nano-NMR detection of ^1H spins using ^{14}NV . (a) Optically detected magnetic resonance (ODMR) spectra of a ^{14}NV centre measured as a function of the axial magnetic field strength, B , near the GSLAC. Solid lines overlaid on the graph are the calculated NV (black lines) and ^1H (green line) spin transitions. (b) T_1 -NMR spectrum around the ^1H resonance, obtained with evolution times $\tau = 1 \mu\text{s}$ (black data) and $\tau = 200 \mu\text{s}$ (red data), plotted as a function of the detuning $\omega_{\text{NV}} - \omega_H$, where ω_{NV} is obtained from fitting the ODMR spectrum and ω_H is the ^1H Larmor frequency. The PL is measured at the start of the readout pulse and normalized by the back of the same pulse. Solid lines are fits to equations (2) and (3). (c) Full T_1 curves measured on resonance ($\omega_{\text{NV}} = 4.4$ MHz, blue data) and off resonance ($\omega_{\text{NV}} = 2.7$ MHz, grey data). Solid lines are fits to equation (2). Error bars represent the photon shot noise (one s.d.) corresponding to $\approx 40,000$ photons within the signal integration window. Horizontal error bars in **b,c** are not shown as they are smaller than the data points.

equation (2), provided I_0 and C are initially calibrated via measurement of a full decay trace $I_{\text{PL}}(\tau, B)$ at a given B . Such a single-point T_1 measurement is done via an initialize, wait, and read-out scheme (Fig. 1c), without any microwave pulsing of either the NV spin or target spin. We note that the relaxation rate induced by each target spin, expressed by equation (1), has a different overall angular dependence for the two resonances before and after the GSLAC, as illustrated in Fig. 1d. This difference allows θ to be inferred, in the case of a single target spin, by directly comparing the transition strengths on either side of the GSLAC.

The simplified picture of resonances near the GSLAC shown in Fig. 1b is in reality modified by hyperfine interactions within the NV centre, associated with the nitrogen nuclear spin which is either ^{14}N (spin-1) or ^{15}N (spin-1/2)^{36–38}. While sensing experiments generally use implanted ^{15}NV centres, as they can be distinguished from native centres of the most abundant isotope,

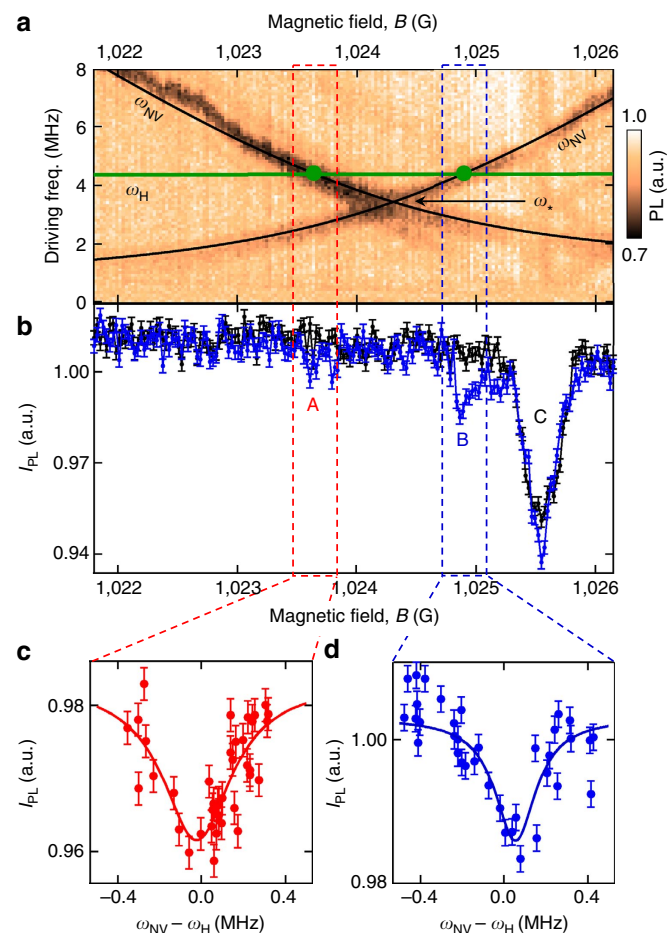


Figure 3 | Nano-NMR detection of ^1H spins using ^{15}NV . (a) ODMR spectra of a ^{15}NV centre measured as a function of B near the GSLAC. The black lines are the calculated frequencies of the two dominant NV spin transitions, which cross at a frequency ω_* (indicated by the black arrow). The frequency of the upper NV transition at each B is denoted as ω_{NV} . The green line indicates the ^1H transition frequency, ω_H . (b) T_1 -NMR spectrum recorded with evolution times $\tau = 1 \mu\text{s}$ (black data) and $\tau = 20 \mu\text{s}$ (blue data). The three features observed are labelled A, B and C. (c,d) T_1 -NMR spectra measured around feature A with $\tau = 100 \mu\text{s}$ (c) and around feature B with $\tau = 20 \mu\text{s}$ (d), plotted against $\omega_{\text{NV}} - \omega_H$, where ω_{NV} is obtained from fitting the ODMR spectrum. Solid lines are fits to equations (2) and (3). Error bars represent the photon shot noise (one s.d.). Horizontal error bars in **c,d** are not shown as they are smaller than the data points.

^{14}N (ref. 39), it has become apparent from recent experiments³⁶ that ^{14}NV and ^{15}NV centres present distinct differences when considering their application for T_1 -NMR spectroscopy due to their different GSLAC electron-nuclear state mixing properties³⁶. For this reason, both isotopic forms of the NV probe were investigated in this work.

Nano-NMR detection of ^1H spins. To demonstrate T_1 -based NMR, a custom-built confocal microscope was used, incorporating a permanent magnet mounted on a 3-axis scanning stage to precisely control the applied background field³⁵. The diamond sample comprises a high purity CVD homoepitaxial layer, grown in a Seki AX6500 diamond reactor. The sample was implanted firstly with 3.5 keV $^{15}\text{N}^+$ ions and then with 3.5 keV $^{14}\text{N}^+$ ions (expected implantation depth in the range 5–15 nm (ref. 40)). Both implants were done to a dose of $0.5 \times 10^9 \text{ cm}^{-2}$ and this was followed by annealing in vacuum at 800 °C and acid cleaning in a boiling mixture of sulfuric acid and sodium nitrate. The diamond has a (100) surface, so that the NV centres have their symmetry axis at 54.7° to the surface normal (Fig. 1a,d). The NV centres were identified as either ^{15}NV or ^{14}NV via their characteristic hyperfine splittings under low-power optically detected magnetic resonance (ODMR)^{39,41}. As a standard proton sample, we used either the oil employed with the oil-immersion objective lens, or a layer of Poly(methyl methacrylate) (PMMA) deposited on the diamond surface^{11,12}.

We first report the results of T_1 -NMR using a ^{14}NV centre. The ODMR spectrum as a function of the background field strength (B) around 1024 G is shown in Fig. 2a, revealing a characteristic GSLAC structure resulting from hyperfine couplings and dynamic polarization of the NV nuclear spin^{36,42}. The NV transitions are shown as black lines, while the ^1H spin transition is shown in green and corresponds to a Larmor frequency $\omega_{\text{H}} \approx 4.4 \text{ MHz}$ in this range of fields. Due to the NV avoided crossing before the GSLAC, there is only one measurable resonance point with ^1H (green dot in Fig. 2a). To probe this resonance, the PL intensity is measured as a function of B , using evolution times $\tau = 1 \mu\text{s}$, which serves as reference for normalization (as no T_1 decay is expected at such time scale), and $\tau = 200 \mu\text{s}$, optimized to probe the ^1H resonance. In the instance of an unknown signal frequency and strength, a scan with an

evolution time of $\frac{T_1}{2}$ would give optimal signal in the low-signal regime. The resulting T_1 -NMR spectrum is shown in Fig. 2b, plotted against the detuning $\omega_{\text{NV}} - \omega_{\text{H}}$, where ω_{NV} is the NV transition frequency obtained from fitting the ODMR spectrum. A dip in the $\tau = 200 \mu\text{s}$ data is clearly observed at the expected ^1H frequency. Full T_1 curves measured on resonance ($\omega_{\text{NV}} = 4.4 \text{ MHz}$) and off resonance ($\omega_{\text{NV}} = 2.7 \text{ MHz}$) are shown in Fig. 2c, confirming a change in relaxation time. Fitting the two curves to equation (2) yields the values $\Gamma_{\text{int}} = 2.1 \pm 0.2 \times 10^3 \text{ s}^{-1}$ and $\Gamma_{\text{ext}} = 5.9 \pm 0.6 \times 10^3 \text{ s}^{-1}$. The proton signal was confirmed to be associated primarily with the immersion oil, as the signal significantly reduced upon removal of the oil (Supplementary Note 4).

We now demonstrate T_1 -NMR using a ^{15}NV centre from the same diamond and proton sample (immersion oil) as was used in the ^{14}NV case. In ref. 36, it has been shown that a typical ^{15}NV exhibits two potential resonances with ^1H , before and after the GSLAC, but that the stronger after-GSLAC resonance overlaps with a feature intrinsic to the GSLAC structure. To circumvent this problem and allow the two resonances to be observed, we selected a ^{15}NV centre exhibiting a hyperfine coupling (here of $\approx 4 \text{ MHz}$) to a nearby ^{13}C , thereby shifting the intrinsic feature away from the NV-proton resonance⁴³ (Supplementary Note 2). The results for this particular ^{15}NV centre are shown in Fig. 3. The ODMR spectrum as a function of B around 1024 G is shown in Fig. 3a, revealing the characteristic ^{15}NV GSLAC structure³⁶. The two dominant transitions (black lines) cross at a frequency $\omega_{\text{H}} \approx 3.5 \text{ MHz}$, which is lower than the Larmor frequency of ^1H in this range of fields (ω_{H} , green line). For each value of B , we define ω_{NV} as the NV transition frequency of the upper branch, that is, $\omega_{\text{NV}} > \omega_{\text{H}}$. The two expected ^1H resonance points, $\omega_{\text{NV}} = \omega_{\text{H}}$, are shown as green dots in Fig. 3a. A T_1 -NMR spectrum recorded using evolution times $\tau = 1 \mu\text{s}$ (reference) and $\tau = 20 \mu\text{s}$ is shown in Fig. 3b and reveals three main features, labelled A, B and C. The first two dips (A and B) are seen only for $\tau = 20 \mu\text{s}$ and correspond to the cross-relaxation resonances with ^1H . The third dip, (C), exhibiting a far stronger decay, which is also visible at short time $\tau = 1 \mu\text{s}$, corresponds to the intrinsic feature discussed above³⁶.

From Fig. 3b, it can be seen that the lower-field ^1H resonance (feature A) is significantly weaker than the higher-field

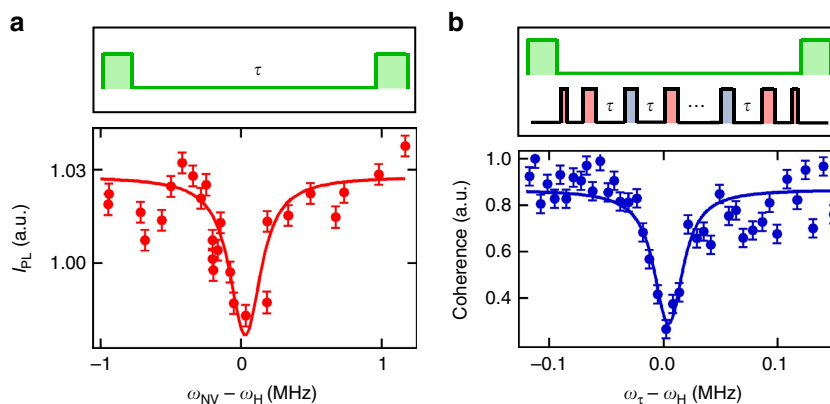


Figure 4 | Comparison of microwave-free T_1 -NMR to the XY8 protocol. (a,b) Spectra from Poly(methyl methacrylate) (PMMA) obtained with a single ^{14}NV centre by using: (a) microwave-free T_1 relaxometry after the GSLAC, with a probe time $\tau = 100 \mu\text{s}$; (b) an XY8- N dynamical decoupling sequence with $N = 256$ microwave pulses at a field $B = 300 \text{ G}$. The corresponding pulse sequence is depicted with laser pulses in green and microwave pulses in red or blue corresponding to 0° or 90° relative phase. In a, the spectrum is constructed by varying the NV frequency, ω_{NV} , via varying the magnetic field strength. In b, it is constructed by scanning the probe frequency $\omega_{\tau} = \pi/\tau$, where τ is the inter-pulse delay, inclusive of the finite π pulse duration. Error bars represent the photon shot noise (one s.d.). Horizontal error bars are not shown as they are smaller than the data points. By fitting the data to the theoretical decay caused by a semi-infinite layer of hydrogen spins we can estimate the distance, d , of the NV centre below the surface (Supplementary Note 3). This gives $d = 10.7 \pm 0.1 \text{ nm}$ for the data in a and $d = 10.5 \pm 0.1 \text{ nm}$ for the data in b.

resonance (feature B). To resolve this resonance more clearly, a longer evolution time, $\tau = 100 \mu\text{s}$, was employed resulting in the spectrum shown in Fig. 3c plotted against the detuning $\omega_{\text{NV}} - \omega_{\text{H}}$. Fitting the data to equation (2) along with equation (3) gives $\Gamma_{1,\text{int}} = 1.5 \pm 0.4 \times 10^3 \text{ s}^{-1}$ and $\Gamma_{1,\text{ext}}^- = 1.5 \pm 0.3 \times 10^3 \text{ s}^{-1}$ for this resonance. Similarly, the spectrum around the ^1H resonance past the GSLAC (Fig. 3d) is fitted to give $\Gamma_{1,\text{int}} = 1.3 \pm 0.2 \times 10^3 \text{ s}^{-1}$ and $\Gamma_{1,\text{ext}}^+ = 5.2 \pm 0.6 \times 10^3 \text{ s}^{-1}$. The measured ratio between the extrinsic relaxation rates of the two resonances is $\frac{\Gamma_{1,\text{ext}}^+}{\Gamma_{1,\text{ext}}^-} \approx 3.5$. This is in qualitative agreement with the ratio of 6.3 predicted by integrating equation (1) over a semi-infinite bath of protons on a (100) surface. This calculation neglects the effects of state mixing due to the GSLAC structure. It has previously been shown that under optimized conditions it would take ≈ 5 min of integration to detect a single proton at a distance of 4 nm showing that single proton detection via T_1 -NMR is possible on realistic experimental timescales³⁵.

Comparison to T_2 -based NMR. We now report a theoretical and experimental comparison of T_1 -NMR spectroscopy to the prevailing existing technique of T_2 -based spectroscopy, which relies on locking a dynamical decoupling pulse sequence on the NV electronic spin state (usually XY8- N where N is the number of microwave π pulses) to the nuclear spins' Larmor frequency^{12–15,44}. Theoretically, the sensitivity can be compared by examining the signal-to-noise ratio (SNR) derived under the identical conditions of a shallow NV centre detecting an ensemble of nuclear spins as in the geometry of Fig. 1a. In the small signal regime (that is, $\Gamma_{\alpha,\text{ext}} \ll \Gamma_{\alpha,\text{int}}$ with $\alpha=1$ for T_1 and $\alpha=2$ for T_2), we find that the maximum SNR in T_1 and T_2 sensing schemes can be expressed as (Supplementary Note 3)

$$\text{SNR}_{T_1,\text{max}} \approx \mathcal{A} \times \frac{19\pi e^{-1/2}}{96\sqrt{2}} \times T_2^* \sqrt{T_1} \quad (4)$$

$$\text{SNR}_{T_2,\text{max}} \approx \mathcal{A} \times \frac{5(3/e)^{3/4}}{48\pi 2^{3/2}} \times (T_2)^{3/2}, \quad (5)$$

respectively, where $T_2^* = 1/\Gamma_2^*$, $T_1 = 1/\Gamma_{1,\text{int}}$ and $T_2 = 1/\Gamma_{2,\text{int}}$ are the intrinsic characteristic times of the NV centre. Note that here T_2 is the extended decoherence time under the considered dynamical decoupling sequence⁴⁵. The constant \mathcal{A} is given by

$$\mathcal{A} = \sqrt{\mathcal{R} T_{\text{tot}} t_{\text{ro}}} C \frac{\rho}{d^3} \left(\frac{\mu_0 \gamma_{\text{NV}} \gamma_{\text{I}} \hbar}{4\pi} \right)^2 \quad (6)$$

where \mathcal{R} is the photon count rate under continuous laser excitation, $t_{\text{ro}} = 300 \text{ ns}$ is the read-out time per pulse, T_{tot} is the total experiment time, ρ is the proton density in the semi-infinite sample, and d is the NV depth. Evaluating the numeric factors, we obtain the ratio between the SNRs,

$$\frac{\text{SNR}_{T_1,\text{max}}}{\text{SNR}_{T_2,\text{max}}} \approx 21.1 \times \frac{T_2^* \sqrt{T_1}}{(T_2)^{3/2}}. \quad (7)$$

For a near-surface NV centre in a bulk diamond ($d \approx 10 \text{ nm}$), typical approximate values are $T_2^* = 2 \mu\text{s}$, $T_1 = 2 \text{ ms}$ and $T_2 = 200 \mu\text{s}$, which yields a ratio $\frac{\text{SNR}_{T_1,\text{max}}}{\text{SNR}_{T_2,\text{max}}} \sim 1$. In other words, our microwave-free T_1 -based NMR spectroscopy technique is similarly sensitive to the existing T_2 -based approach without requiring complex microwave pulse sequences. This theoretical comparison assumes a stable magnetic field in both cases.

To verify this and further compare the two approaches, we conducted a comparative measurement using a single shallow ^{14}NV centre, where the diamond was coated with a layer of PMMA. Figure 4 shows the hydrogen spectrum measured via T_1

relaxometry (a) and via an XY8-256 sequence (b). Both spectra were acquired in a total time of about 2 h, and show a clear feature at the ^1H frequency with a similar signal-to-noise ratio. In addition, one can compare the NV depth, d , inferred through fitting the appropriately normalized data from each method, assuming the signal comes from a semi-infinite bath of protons on a (100) surface (see Supplementary Notes 1 and 3). Using a proton density of $\rho = 56 \text{ nm}^{-3}$, we find $d = 10.7 \pm 0.1 \text{ nm}$ from the T_1 data, against $d = 10.5 \pm 0.1 \text{ nm}$ from the XY8 data, indicating a high level of consistency between the two approaches. From the inferred depth, we deduce that 50% of the signal is generated by the $\approx 6 \times 10^4$ closest protons, corresponding to a detection volume of about $(10 \text{ nm})^3$ (refs 12,13).

The spectral resolution of T_1 spectroscopy, however, is currently limited by the dephasing rate $\Gamma_2^* = 1/T_2^*$ (equation (3)), while it is limited by T_2 with the XY8 method, and can be improved further using correlation spectroscopy^{46–48}. We note that both the sensitivity and spectral resolution of the T_1 approach could be dramatically improved by optimizing T_2^* , which motivates further work towards understanding and mitigating the decoherence of near-surface NV centres^{49–51}.

Discussion

In summary, we have demonstrated the detection of proton spins external to a diamond using a microwave-free nano-NMR technique based on T_1 relaxometry of a single NV centre. While the electron-nuclear spin physics near the NV GSLAC are relatively complex, we have shown that the microwave-free T_1 protocol can nevertheless be implemented and the ^1H resonances observed, which we have demonstrated using both isotopic forms of the NV centre. In addition, we have shown a sensitivity comparable to an existing nano-NMR protocol which requires quantum state manipulation via microwave excitation. The sensitivity as well as the spectral resolution of our approach could be improved via engineering of the diamond surface. We note that the resulting all-optical technique can be implemented using non-invasive excitation constrained within the diamond, using total internal reflection. The removal of microwave quantum control eliminates the possibility of spurious harmonics within the measurement and opens up applications in areas where such control is inherently difficult to achieve and/or invasive, such as spectroscopic imaging over wide fields of view or in scanning probe microscopy experiments. Finally, it is worth mentioning that the demonstrated T_1 protocol can be used not only for sensing but also to hyperpolarise the target nuclear spins via spin transfer, which may have important applications in medical NMR.

Data availability. All relevant data are available from the authors on request.

References

- Doherty, M. W. *et al.* The nitrogen-vacancy colour centre in diamond. *Phys. Rep.* **528**, 1–45 (2013).
- Chernobrod, B. M. & Berman, G. P. Spin microscope based on optically detected magnetic resonance. *J. Appl. Phys.* **97**, 014903 (2005).
- Degen, C. L. Scanning magnetic field microscope with a diamond single-spin sensor. *Appl. Phys. Lett.* **92**, 243111 (2008).
- Taylor, J. M. *et al.* High-sensitivity diamond magnetometer with nanoscale resolution. *Nat. Phys.* **4**, 810–816 (2008).
- Balasubramanian, G. *et al.* Nanoscale imaging magnetometry with diamond spins under ambient conditions. *Nature* **455**, 648–651 (2008).
- Maze, J. R. *et al.* Nanoscale magnetic sensing with an individual electronic spin in diamond. *Nature* **455**, 644–647 (2008).
- Cole, J. H. & Hollenberg, L. C. L. Scanning quantum decoherence microscopy. *Nanotechnology* **20**, 495401 (2009).

8. Hall, L. T., Cole, J. H., Hill, C. D. & Hollenberg, L. C. L. Sensing of fluctuating nanoscale magnetic fields using nitrogen-vacancy centers in diamond. *Phys. Rev. Lett.* **103**, 220802 (2009).
9. Rondin, L. *et al.* Magnetometry with nitrogen-vacancy defects in diamond. *Rep. Prog. Phys.* **77**, 056503 (2014).
10. Schirhagl, R., Chang, K., Loretz, M. & Degen, C. L. Nitrogen-vacancy centers in diamond: nanoscale sensors for physics and biology. *Annu. Rev. Phys. Chem.* **65**, 83–105 (2014).
11. Mamin, H. J. *et al.* Nanoscale nuclear magnetic resonance with a nitrogen-vacancy spin sensor. *Science* **339**, 557–560 (2013).
12. Staudacher, T. *et al.* Nuclear magnetic resonance spectroscopy on a (5-nanometer)³ sample volume. *Science* **339**, 561–563 (2013).
13. Loretz, M., Pezzagna, S., Meijer, J. & Degen, C. L. Nanoscale nuclear magnetic resonance with a 1.9-nm-deep nitrogen-vacancy sensor. *Appl. Phys. Lett.* **104**, 033102 (2014).
14. Muller, C. *et al.* Nuclear magnetic resonance spectroscopy with single spin sensitivity. *Nat. Commun.* **5**, 4703 (2014).
15. DeVience, S. J. *et al.* Nanoscale NMR spectroscopy and imaging of multiple nuclear species. *Nat. Nano* **10**, 129–134 (2015).
16. Lovchinsky, I. *et al.* Nuclear magnetic resonance detection and spectroscopy of single proteins using quantum logic. *Science* **351**, 836–841 (2016).
17. McGuinness, L. P. *et al.* Quantum measurement and orientation tracking of fluorescent nanodiamonds inside living cells. *Nat. Nano* **6**, 358–363 (2011).
18. Shi, F. *et al.* Single-protein spin resonance spectroscopy under ambient conditions. *Science* **347**, 1135–1138 (2015).
19. Loretz, M. *et al.* Spurious harmonic response of multipulse quantum sensing sequences. *Phys. Rev. X* **5**, 021009 (2015).
20. Wickenbrock, A. *et al.* Microwave-free magnetometry with nitrogen-vacancy centers in diamond. *Appl. Phys. Lett.* **109**, 053505 (2016).
21. Simpson, D. A. *et al.* Magneto-optical imaging of thin magnetic films using spins in diamond. *Sci. Rep.* **6**, 22797 (2016).
22. Maletinsky, P. *et al.* A robust scanning diamond sensor for nanoscale imaging with single nitrogen-vacancy centres. *Nat. Nano* **7**, 320–324 (2012).
23. Tetienne, J.-P. *et al.* Nanoscale imaging and control of domain-wall hopping with a nitrogen-vacancy center microscope. *Science* **344**, 1366–1369 (2013).
24. Tetienne, J.-P. *et al.* Scanning nanospin ensemble microscope for nanoscale magnetic and thermal imaging. *Nano Lett.* **16**, 326–333 (2016).
25. Hall, L. T. *et al.* Detection of nanoscale electron spin resonance spectra demonstrated using nitrogen-vacancy centre probes in diamond. *Nat. Commun.* **7**, 10211 (2016).
26. Clevenson, H. *et al.* Broadband magnetometry and temperature sensing with a light-trapping diamond waveguide. *Nat. Phys.* **11**, 393–397 (2015).
27. Kaufmann, S. *et al.* Detection of atomic spin labels in a lipid bilayer using a single-spin nanodiamond probe. *Proc. Natl Acad. Sci. USA* **110**, 10894 (2013).
28. Steinert, S. *et al.* Magnetic spin imaging under ambient conditions with sub-cellular resolution. *Nat. Commun.* **4**, 1607 (2013).
29. Tetienne, J.-P. *et al.* Spin relaxometry of single nitrogen-vacancy defects in diamond nanocrystals for magnetic noise sensing. *Phys. Rev. B* **87**, 235436 (2013).
30. Sushkov, A. O. *et al.* All-optical sensing of a single-molecule electron spin. *Nano Lett.* **14**, 6443–6448 (2014).
31. Holliday, K., Manson, N. B., Glasbeek, M. & Van Oort, E. Optical hole-bleaching by level anti-crossing and cross relaxation in the N-V centre in diamond. *J. Phys. Condens. Matter* **1**, 7093 (1989).
32. Armstrong, S., Rogers, L. J., McMurtrie, R. L. & Manson, N. B. NV-NV electron-electron spin and NV-N₅ electron-electron and electron-nuclear spin interaction in diamond. *Phys. Procedia* **3**, 1569–1575 (2010).
33. Jarmola, A., Acosta, V. M., Jensen, K., Chemerisov, S. & Budker, D. Temperature- and magnetic-field-dependent longitudinal spin relaxation in nitrogen-vacancy ensembles in diamond. *Phys. Rev. Lett.* **108**, 197601 (2012).
34. Wang, H.-J. *et al.* Optically detected cross-relaxation spectroscopy of electron spins in diamond. *Nat. Commun.* **5**, 4135 (2014).
35. Wood, J. D. A. *et al.* Wide-band, nanoscale magnetic resonance spectroscopy using quantum relaxation of a single spin in diamond. *Phys. Rev. B* **94**, 155402 (2016).
36. Broadway, D. A. *et al.* Anticrossing spin dynamics of diamond nitrogen-vacancy centers and all-optical low-frequency magnetometry. *Phys. Rev. Appl.* **6**, 064001 (2016).
37. He, X.-F., Manson, N. B. & Fisk, P. T. H. Paramagnetic resonance of photoexcited N-V defects in diamond. I. Level anticrossing in the ³A ground state. *Phys. Rev. B* **47**, 8809 (1993).
38. Epstein, R. J., Mendoza, F. M., Kato, Y. K. & Awschalom, D. D. Anisotropic interactions of a single spin and dark-spin spectroscopy in diamond. *Nat. Phys.* **1**, 94–98 (2005).
39. Rabeau, J. R. *et al.* Implantation of labelled single nitrogen vacancy centers in diamond using ¹⁵N. *Appl. Phys. Lett.* **88**, 023113 (2006).
40. Lehtinen, O. *et al.* Molecular dynamics simulations of shallow nitrogen and silicon implantation into diamond. *Phys. Rev. B* **93**, 35202 (2016).
41. Dréau, A. *et al.* Avoiding power broadening in optically detected magnetic resonance of single NV defects for enhanced dc magnetic field sensitivity. *Phys. Rev. B* **84**, 195204 (2011).
42. Jacques, V. *et al.* Dynamic polarization of single nuclear spins by optical pumping of nitrogen-vacancy color centers in diamond at room temperature. *Phys. Rev. Lett.* **102**, 057403 (2009).
43. Dréau, A., Maze, J. R., Lesik, M., Roch, J.-F. & Jacques, V. High-resolution spectroscopy of single NV defects coupled with nearby ¹³C nuclear spins in diamond. *Phys. Rev. B* **85**, 134107 (2012).
44. Pham, L. M. *et al.* NMR technique for determining the depth of shallow nitrogen-vacancy centers in diamond. *Phys. Rev. B* **93**, 045425 (2015).
45. Pham, L. M. *et al.* Enhanced solid-state multispin metrology using dynamical decoupling. *Phys. Rev. B* **86**, 045214 (2012).
46. Staudacher, T. *et al.* Probing molecular dynamics at the nanoscale via an individual paramagnetic centre. *Nat. Commun.* **6**, 8527 (2015).
47. Kong, X., Stark, A., Du, J., McGuinness, L. P. & Jelezko, F. Towards chemical structure resolution with nanoscale nuclear magnetic resonance spectroscopy. *Phys. Rev. Appl.* **4**, 024004 (2015).
48. Boss, J. M. *et al.* One- and two-dimensional nuclear magnetic resonance spectroscopy with a diamond quantum sensor. *Phys. Rev. Lett.* **116**, 197601 (2016).
49. Myers, B. A. *et al.* Probing surface noise with depth-calibrated spins in diamond. *Phys. Rev. Lett.* **113**, 027602 (2014).
50. Rosskopf, T. *et al.* Investigation of surface magnetic noise by shallow spins in diamond. *Phys. Rev. Lett.* **112**, 147602 (2014).
51. Romach, Y. *et al.* Spectroscopy of surface-induced noise using shallow spins in diamond. *Phys. Rev. Lett.* **114**, 017601 (2015).

Acknowledgements

This work was supported in part by the Australian Research Council (ARC) under the Centre of Excellence scheme (Project No. CE110001027). L.C.L.H. acknowledges the support of an ARC Laureate Fellowship (Project No. FL130100119). This work was supported in part by the Melbourne Centre for Nanofabrication (MCN) in the Victorian Node of the Australian National Fabrication Facility (ANFF).

Author contributions

L.T.H. and L.C.L.H. conceived and developed the theory of T_1 -NMR. J.D.A.W. and A.S. planned the experiment. D.A.S. and A.S. prepared the diamond samples and assisted in the experimental setup. J.D.A.W., J.-P.T. and D.A.B. conducted the experiments. J.D.A.W. and J.-P.T. analysed the data. L.C.L.H. supervised the project. All authors discussed the results and participated in writing the manuscript.

Additional information

Supplementary Information accompanies this paper at <http://www.nature.com/naturecommunications>

Competing interests: The authors declare no competing financial interests.

Reprints and permission information is available online at <http://npg.nature.com/reprintsandpermissions/>

How to cite this article: Wood, J. D. A. *et al.* Microwave-free nuclear magnetic resonance at molecular scales. *Nat. Commun.* **8**, 15950 doi: 10.1038/ncomms15950 (2017).

Publisher's note: Springer Nature remains neutral with regard to jurisdictional claims in published maps and institutional affiliations.



Open Access This article is licensed under a Creative Commons Attribution 4.0 International License, which permits use, sharing, adaptation, distribution and reproduction in any medium or format, as long as you give appropriate credit to the original author(s) and the source, provide a link to the Creative Commons license, and indicate if changes were made. The images or other third party material in this article are included in the article's Creative Commons license, unless indicated otherwise in a credit line to the material. If material is not included in the article's Creative Commons license and your intended use is not permitted by statutory regulation or exceeds the permitted use, you will need to obtain permission directly from the copyright holder. To view a copy of this license, visit <http://creativecommons.org/licenses/by/4.0/>

© The Author(s) 2017